MRS Advances (2021) 6:112–118
https://doi.org/10.1557/s43580-021-00055-8

ORIGINAL PAPER

# Synthesis and characterisation of HIP $Ca_{0.80}Ce_{0.20}ZrTi_{1.60}Cr_{0.40}O_7$ zirconolite and observations of the ceramic–canister interface

Lewis R. Blackburn[1] · Max R. Cole[1] · Laura J. Gardner[1] · Daniel J. Bailey[1] · Merve Kuman[1] · Amber R. Mason[1] · Shi-Kuan Sun[1] · Ewan R. Maddrell[2] · Martin C. Stennett[1] · Claire L. Corkhill[1] · Neil C. Hyatt[1]

Received: 24 December 2020 / Accepted: 2 April 2021 / Published online: 16 April 2021


## Abstract

A sample of zirconolite with nominal composition $Ca_{0.80}Ce_{0.20}ZrTi_{1.60}Cr_{0.40}O_7$ was processed via Hot Isostatic Pressing (HIP), with a dwell temperature and pressure of 1320 °C/100 MPa maintained for 4 h. The produced wasteform was characterised by powder XRD, SEM–EDS, Ce $L_3$ and Cr K-edge XANES. A significant portion of the Ce inventory did not fully partition within the zirconolite phase, instead remaining as $CeO_2$ within the microstructure. Inspection of the stainless steel–ceramic interface detailed the presence of an interaction region dominated by a Cr-rich oxide layer. No significant Cr or Fe migration was observed, although a greater concentration of perovskite was observed at the periphery, relative to the bulk ceramic matrix. The X-ray absorption features of Cr remained analogous with $Cr^{3+}$ accommodation within $TiO_6$ octahedra in the zirconolite matrix. The absorption edge of Ce was comprised of contributions from zirconolite-2M and unincorporated $CeO_2$, with an average oxidation state of $Ce^{3.9+}$. As zirconolite-2M accounted for > 92 wt% of the overall phase assemblage, it is clear that the dominant oxidation state of Ce in this phase was $Ce^{4+}$.

## Introduction

In the United Kingdom, aqueous reprocessing of spent nuclear fuel (SNF) has afforded a significant inventory of $PuO_2$, forecast to amount to 140 teHM (tonnes heavy metal equivalent), representing a significant decommissioning effort and a unique challenge with respect materials degradation [1]. Immobilisation of the bulk Pu inventory through a campaign of hot isostatic pressing (HIP), prior to geological disposal, is considered a credible pathway to disposition. Zirconolite ceramics (ideally $CaZrTi_2O_7$) are considered a potential host matrix for immobilisation of Pu; the crystal structure may accept a wide variety of tri- and tetravalent rare earth and actinide species in solid solution, with aqueous durability superior to that of closely related pyrochlore ($Gd_2Ti_2O_7$) and brannerite ($UTi_2O_6$) phases [2]. Zirconolite is considered to be a derivative of the anion-deficient fluorite superstructure, with the parent zirconolite-2M structure crystallising with monoclinic symmetry over the compositional range $CaZr_xTi_{3-x}O_7$ ($0.8 < x < 1.3$), in the space group C2/c [3]. The aristotype is comprised of alternating layers of $Ca^{2+}$ and $Zr^{4+}$ cation polyhedra, coordinated 8- and sevenfold to oxygen, respectively, interspaced with corner sharing $TiO_6$ arranged in a topology similar to that of hexagonal tungsten bronze (HTB). Zirconolite may accept actinide cations, such as $Pu^{4+}$ in solid solution via isovalent substitution i.e. $CaZr_{1-x}Pu_xTi_2O_7$ or by a coupled substitution by which $Pu^{4+}$ is accommodated in the $Ca^{2+}$ site, facilitated by the incorporation of a lower valence charge balancing species e.g. $Ca_{1-x}Pu_xZrTi_{2-2x}Cr_{2x}O_7$. We recently investigated the feasibility of $Cr^{3+}$ as a charge balancing species, targeting $Ca_{1-x}Ce_xZrTi_{2-2x}Cr_{2x}O_7$, utilising Ce as a Pu surrogate, through two distinct ceramic processing routes: a conventional cold press and sinter method (CPS), and a novel reactive spark plasma sintering (RSPS) methodology [4]. Whilst the CPS route yielded a single phase product in the range $0.05 \leq x \leq 0.15$, further substitution of Ce promoted the formation of a Ce-rich perovskite ($CaTiO_3$) phase, facilitated by partial $Ce^{3+}$ speciation, and unincorporated $CeO_2$ and $Cr_2O_3$ above $x = 0.25$. The formation of an accessory perovskite

✉ Lewis R. Blackburn
lewis.blackburn@sheffield.ac.uk

✉ Neil C. Hyatt
n.c.hyatt@sheffield.ac.uk

[1] Immobilisation Science Laboratory, Department of Materials Science and Engineering, University of Sheffield, Sir Robert Hadfield Building, Mappin Street, Sheffield S13JD, UK

[2] National Nuclear Laboratory, Workington CA201PJ, Cumbria, UK

phase would reduce the overall wasteform performance, as this phase is known to exhibit reduced aqueous durability relative to zirconolite [5]. Nevertheless, a yield of ~ 94 wt% zirconolite-2M was obtained when targeting $x = 0.35$, corresponding to approximately 25 wt% Pu loading in the corresponding solid solution. All specimens prepared by the CPS method presented a highly porous microstructure. RSPS was therefore applied to achieve complete sintering, since this technique has previously been utilised to produce zirconolite with near theoretical density [6]. Whilst RSPS produced ceramic bodies with no significant porosity, the conditions were sufficient to entirely reduce the Ce inventory to $Ce^{3+}$, resulting in disruption of the target phase assemblage, favouring Ce-perovskite as an accessory phase. Hot isostatic pressing is the favoured thermal processing route for disposition of the bulk Pu inventory, and has recently been investigated for both zirconolite ceramic and glass–ceramic matrices, using a multitude of Pu surrogates, and indeed Pu validation trials have been performed [7–10]. HIP processing involves the simultaneous application of high temperatures (> 1300 °C) and isostatic pressure (> 100 MPa) via an inert Ar gas medium, to a loosely packed ceramic precursor material pressed into the walls of a hermetically sealed overpack, typically Ni metal or high grade stainless steel. This offers distinct advantages with respect to conventional sintering and RSPS, as the application of isostatic pressure during processing affords elimination of porosity, whilst producing minimal secondary effluent streams and remaining insensitive to the physical and chemical nature of the feedstock material [11]. In the present work, we investigate the feasibility of $Cr^{3+}$ as a charge compensation species, targeting $Ca_{0.80}Ce_{0.20}ZrTi_{1.60}Cr_{0.40}O_7$ as to remain analogous to our previous studies of this system. We also provide a characterisation of the ceramic–canister interface.

## Experimental methods

### Materials synthesis

A zirconolite ceramic with nominal composition $Ca_{0.80}Ce_{0.20}ZrTi_{1.60}Cr_{0.40}O_7$ was fabricated by hot isostatic pressing, with the view to use $Ce^{4+}$ as a structural surrogate for $Pu^{4+}$. This composition was selected since it would afford an approximate 15 wt% incorporation rate of Pu. Commercial metal oxide precursors $CaTiO_3$ (Sigma-Aldrich, > 99.9%), $ZrO_2$ (Sigma-Aldrich, > 99.9%), $CeO_2$ (Acros Organics, > 99.9%), $TiO_2$ (rutile, Sigma-Aldrich, > 99.9%) and $Cr_2O_3$ (Sigma-Aldrich, > 99.9%) were dried and batched according to desired composition, intimately mixed by planetary milling at 500 rpm for 20 min, using $ZrO_2$ milling media and isopropanol as a milling agent. Powder slurries were discharged and dried at 80 °C overnight to evaporate excess solvent, prior to calcination at 600 °C for 12 h. Compositions were then pressed into the walls of a 316 stainless steel HIP canister under uniaxial pressure, ensuring uniform packing density. The HIP canisters were machined with internal diameter 22 mm and can wall thickness of 2 mm. The canisters were then heated under vacuum at 300 °C until an internal canister pressure of ~ 7 Pa was reached, before crimping and welding shut to attain a hermetic seal. The canisters were then placed into a AIP6-30H HIP unit and processed at 1320 °C, with a 100 MPa dwell pressure maintained for 4 h, with inert Ar gas introduced into the pressure vessel as the pressure transfer medium.

### Materials characterisation

The processed canister was retrieved and sectioned using a Buelher IsoMet 1000 low speed saw, with material extracted from the bulk and the stainless steel-ceramic interface preserved for analysis. Powder X-ray diffraction (XRD) analysis was performed using a Bruker D2 Phaser fitted with a Lynxeye position sensitive detector and Ni filter. Data were acquired using a Cu Kα source ($\lambda = 1.5418$ Å) in the range $5° \leq 2\theta \leq 80°$ with a stepsize of 0.02°. Powder XRD data were refined by the Rietveld method, using the GSAS package with EXPGUI interface [12]. The bottom section of the canister was set in epoxy resin and polished to a 1 µm optical finish, permitting microanalysis of both the bulk ceramic material and the exterior can–ceramic interface. Scanning electron microscopy (SEM) analysis was performed using a FEI Inspect f50 operating at 20 kV accelerating voltage and 10.6 mm working distance. Ce $L_3$ and Cr K-edge X-ray absorption near edge spectroscopy (XANES) data were collected at beamline BL-27 at the Photon Factory (PF) accelerator light source (Tsukuba, Japan). The optical arrangement consists of a double crystal Si(111) monochromator and slits were used to reduce the size of the beam to 3 mm in the horizontal and 1 mm in the vertical. Spectra were recorded between 5590–5990 eV and 5523–6154 eV in energy steps of 0.25 eV using an acquisition time of 50 ms $step^{-1}$ for Cr K and Ce $L_3$ edges, respectively. Data were collected alongside a series of reference compounds, representative of Ce and Cr in a variety of valence states and coordination environments.

## Results and discussion

### Characterisation of bulk zirconolite ceramic matrix by XRD and SEM

The HIP processing cycle produced a high density monolith, visually black in colour, with no evidence of loss of containment. Powder XRD data for material retrieved

from the bulk of the HIP can is displayed in Fig. 1. Intense reflections, corresponding in position and intensity to the target zirconolite-2M phase, were identified. The lattice parameters corresponding to the zirconolite-2M phase were calculated by Rietveld refinement to be: $a = 12.4499(7)$ Å, $b = 7.2457(4)$ Å, $c = 11.3798(6)$ Å, $\beta = 100.591(6)°$ and $V = 1009.06(8)$ Å$^3$. Accessory phases $CaTiO_3$ (~ 0.8 wt%), $ZrO_2$ (~ 1.1 wt%), $CeO_2$ (~ 3.9 wt%) and $Cr_2O_3$ (~ 1.9 wt%) were also distinguished (precision ± 0.1 wt%). Whilst the material densified with a comparable quantity of perovskite reported for the corresponding CPS sample (~ 1.2 wt%) [4], incomplete digestion of the $CeO_2$ surrogate inventory within the wasteform was observed to an unsatisfactory degree. SEM analysis of the bulk microstructure detailed a dense morphology consistent with those previously characterised for zirconolite produced by HIP [7]. A matrix of zirconolite-2M was observed with medium grey-scale contrast, with accessory phases clearly distinguished from the bulk through backscattered electron contrast, alongside some minor porosity (black regions in Fig. 2). Relics of undigested $CeO_2$ were clearly evidenced with bright contrast throughout the ceramic matrix, with a clear reaction rim indicating that the reaction did not achieve equilibrium under the imposed HIP conditions. The composition of the reaction rims was consistent with Ce-rich perovskite $(Ca,Ce)TiO_3$, in agreement with powder XRD data, or potentially $CaCeTi_2O_7$, although reflections consistent with this pyrochlore structured phase were not evidenced by diffraction data.

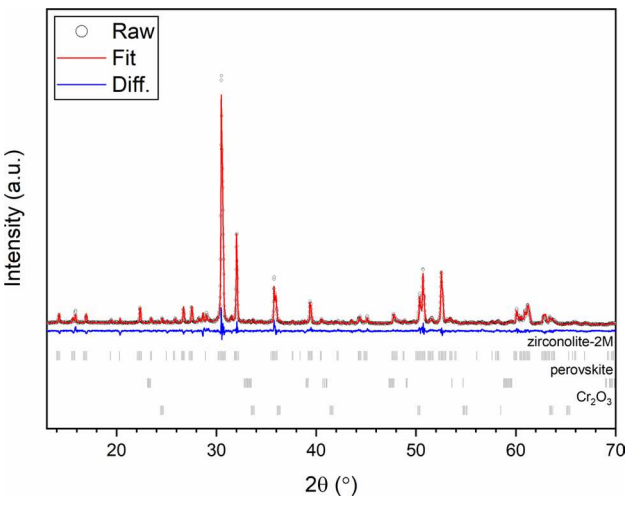


**Fig. 1** Powder XRD data for $Ca_{0.80}Ce_{0.20}ZrTi_{1.60}Cr_{0.40}O_7$ processed via HIP at 1320 °C with a dwell pressure of 100 MPa maintained for 4 h

## Examination of ceramic–canister interface

A cross-sectional backscattered electron micrograph, and corresponding elemental mapping of the interface between the stainless steel HIP-canister and the ceramic matrix is shown in Fig. 3, allowing a detailed interpretation of the interaction region. The interior HIP-can region did not evidence any significant diffusion of constituent elements beyond the layer marked 'interface' in Fig. 3, as demonstrated by Ni and Fe element maps. The HIP can did contain some discrete $Cr_2O_3$ oxides scattered adjacent to the interface. The interface region was consistently measured to be 5–8 µm in width across the specimen, and was dominated in composition by a Cr-rich oxide, with minor Fe and trace Ti evidenced by EDS analysis. The formation of the Cr-rich interface layer was considered to be the effect of Cr/Fe diffusion from the HIP canister and subsequent oxidation, as had been previously described for stainless steel–SYNROC interactions under comparable conditions [13]. Nevertheless, the composition of the interface region was not entirely consistent with those described previously for pyrochlore-rich SYNROC and zirconolite-rich wasteforms. For example, Li et al. confirmed that $Fe^{2+}$ was the main element to diffuse from the can material, partitioning within zirconolite and hollandite ($BaAl_2Ti_6O_{16}$), replacing Ca/Ti and Al, respectively, however it was noted that $Fe^{2+}$ preferentially entered the Ti site in zirconolite [13]. Zhang et al. described similar features, with Fe and Cr diffusion into the zirconolite phase [14]. The composition of the interface region is generally more heterogeneous than the data presented in the present work, dominated by Fe diffusion into the wasteform. For example, Zhang et al. described five distinct subsections of the interface, one of which was rich in Fe adjacent to the bulk ceramic matrix, whereas the interface for $Ca_{0.80}Ce_{0.20}ZrTi_{1.60}Cr_{0.40}O$ appears to be comprised of just three distinct layers [15]. Close inspection of the Fe EDS data did reveal a thin reaction layer rich in Fe relative to Cr, however Fe diffusion did not appear to influence the local chemistry of the zirconolite phase. The distinct lack of an Fe-rich region in the interaction layer is presumably due to the high concentration of Cr present in the wasteform matrix, with subsequent diffusion into the interface. The primary observation from these data is that the diffusion and subsequent oxidation of Cr and Fe from the canister material did not appear to significantly destabilise the local phase assemblage in the ceramic microstructure, although it is evident that undigested $CeO_2$ was concentrated towards the bulk of the ceramic matrix, likely the result of local redox chemistry favouring slightly reducing conditions at the periphery, resulting from Cr and Fe oxidation. The reducing environment may have promoted reduction of the local Ce inventory to $Ce^{3+}$ and subsequent partitioning within a perovskite phase. Moreover, clusters of perovskite

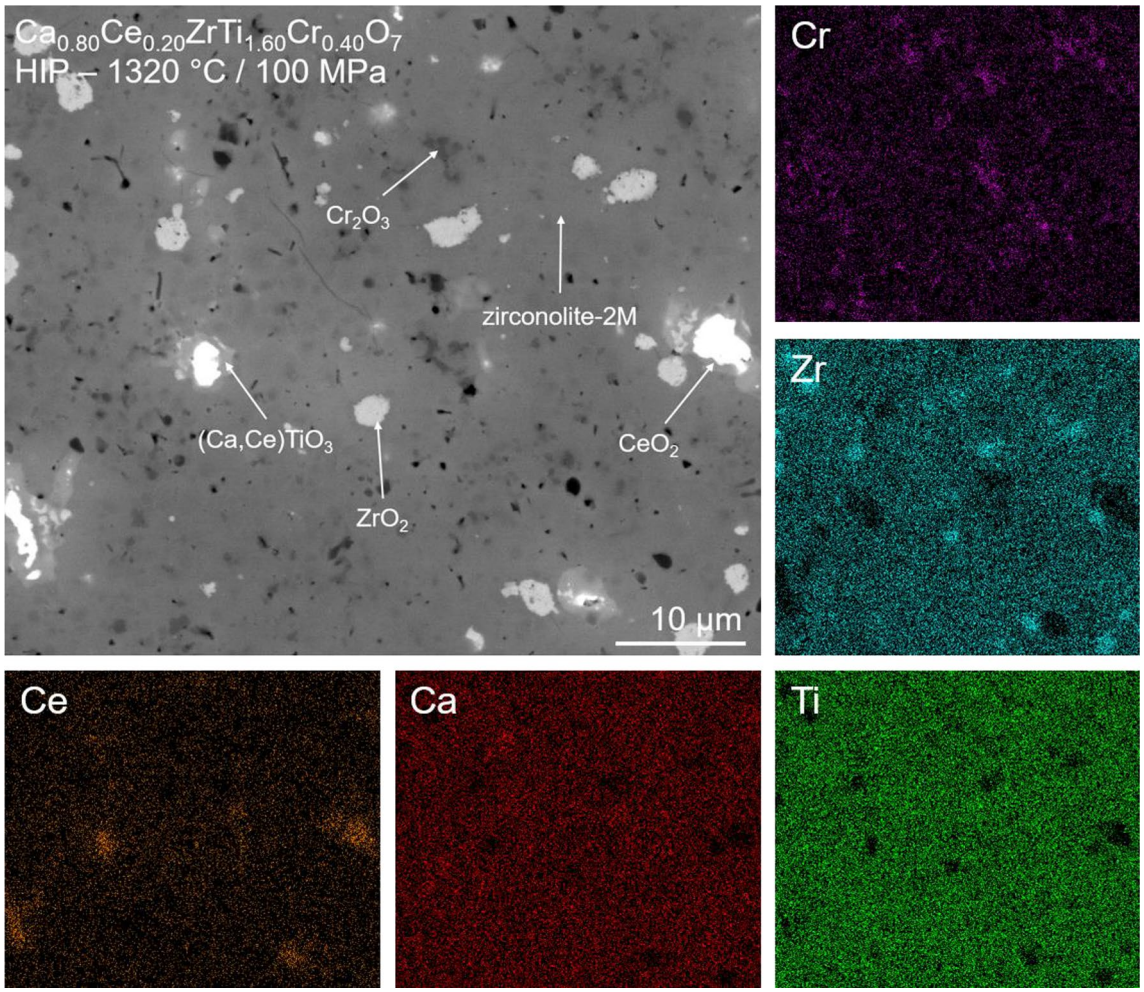


**Fig. 2** SEM–EDS analysis of HIPed $Ca_{0.80}Ce_{0.20}ZrTi_{1.60}Cr_{0.40}O_7$ matrix

appeared more readily formed near the Cr-rich oxide layer, with EDS analysis confirming greater Cr concentration (likely substituted for $Ti^{3+/4+}$ in perovskite) relative to the perovskite reaction rims located around undigested $CeO_2$ in the bulk material. It is important to note, however, that there is no clear indication that the stainless steel–wasteform interface will lead to the formation of non-durable phases or free actinides.

## Cr K- and Ce $L_3$-edge XANES

X-ray absorption spectroscopy (XAS) is a fundamental technique in support of nuclear waste management, as an effective means to probe the local structure and valence chemistry of radionuclides in immobilisation matrices, supporting the safety case towards geological disposal through underpinning the underlying crystal chemistry of actinide-containing wasteforms [16–18]. Accordingly, Ce $L_3$ and Cr K-edge X-ray absorption near edge structure (XANES) data were collected alongside a series of reference compounds representing Ce and Cr in a variety of oxidation states and coordination environments, allowing the speciation and local environment of Ce and Cr to be inferred. Cr K edge XANES is displayed in Fig. 4, alongside $Cr_2O_3$, $YCrO_3$ and $K_2CrO_4$ (representing $Cr^{3+}$, $Cr^{3+}$ and $Cr^{6+}$, respectively). The XANES region for $K_2CrO_4$, in which $Cr^{6+}$ adopts tetrahedral coordination to neighbouring oxygen atoms, was dominated by an intense pre-edge feature, with a centroid position approximately 15 eV from the main absorption edge. This feature was not present in the XANES spectrum for the HIPed zirconolite specimen, inferring the absence of $Cr^{6+}$. Inspection of the Cr K-edge data revealed white line features comparable with $Cr^{3+}$ reference compounds ($YCrO_3$ and $Cr_2O_3$), consistent with a similar edge position and low intensity pre-edge feature [19]. Through modelling of the pre-edge feature, it was previously observed that $Cr^{3+}$ adopts the octahedral coordination in the zirconolite structure, consistent with substitution within $TiO_6$ polyhedra. The absorption features for HIPed $Ca_{0.80}Ce_{0.20}ZrTi_{1.60}Cr_{0.40}O_7$ were consistent with those reported previously for the

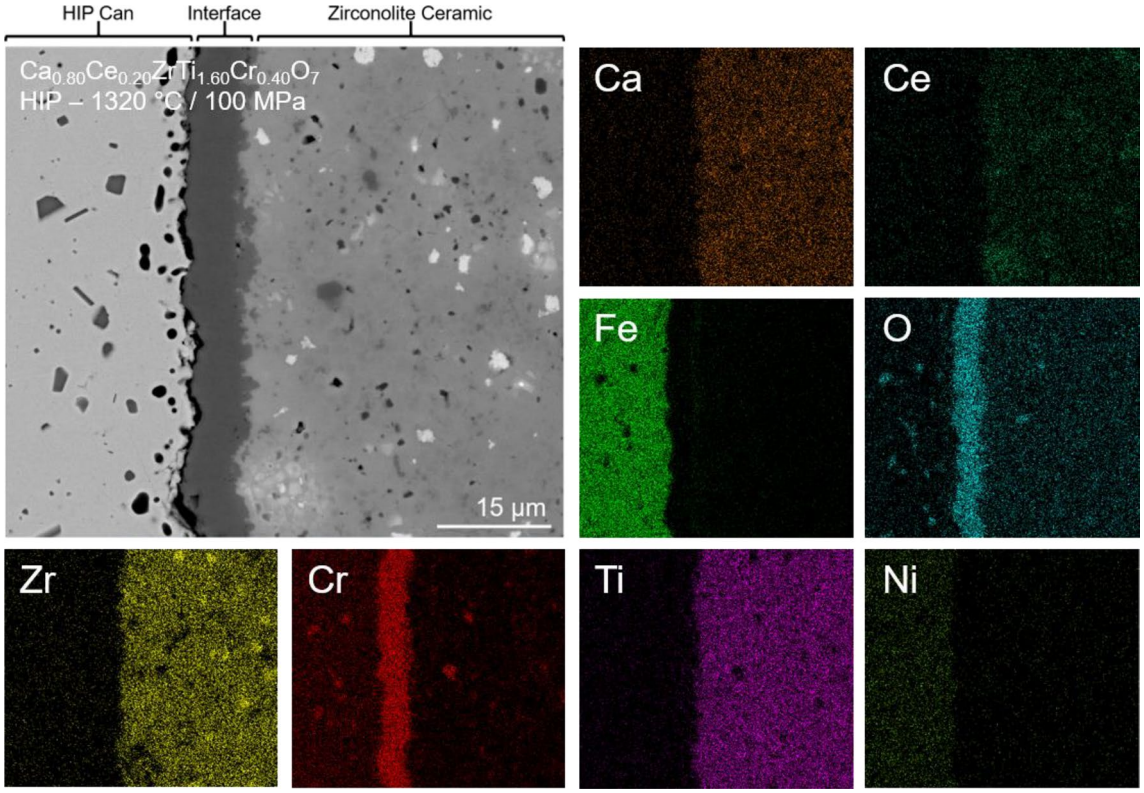


**Fig. 3** Backscattered SEM micrograph and elemental distribution maps for the stainless steel-ceramic interface

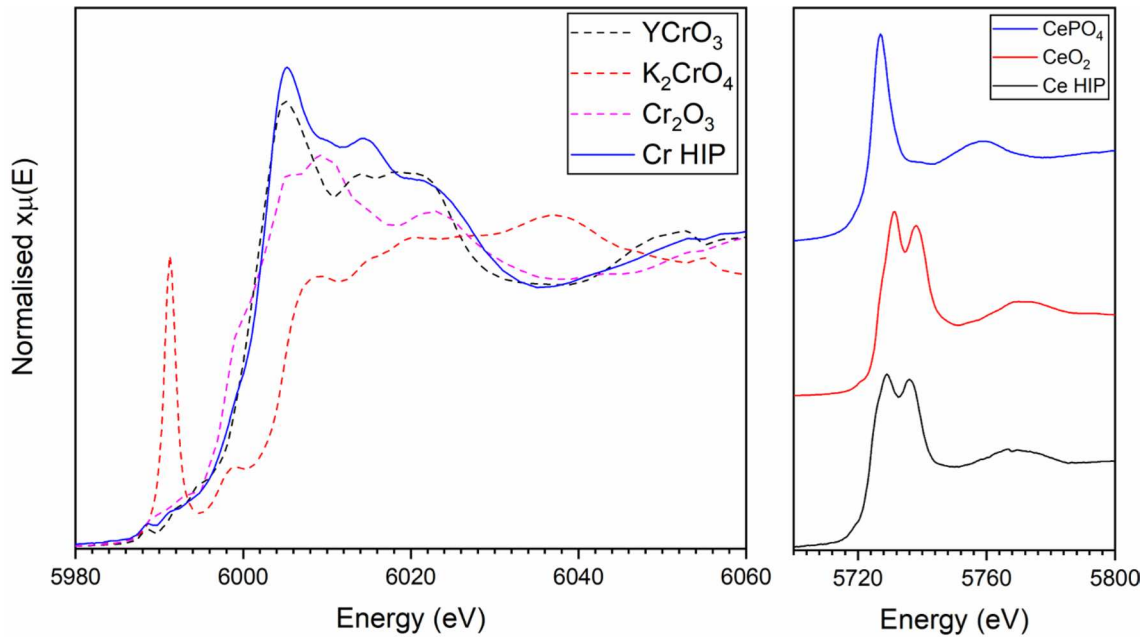


**Fig. 4** Cr K (left) and Ce $L_3$-edge (right) XANES data for HIPed $Ca_{0.80}Ce_{0.20}ZrTi_{1.60}Cr_{0.40}O_7$, alongside $YCr^{3+}O_3$, $K_2Cr^{6+}O_4$, $Cr_2{}^{3+}O_3$, $Ce^{4+}O_2$ and $Ce^{3+}PO_4$ reference compounds

corresponding CPS composition [4], hence by analogy, it can be assumed that the same substitution mechanism occurred for the HIPed sample. Ce $L_3$ XANES were collected alongside $CeO_2$ and $CePO_4$, representing $Ce^{4+}$ and $Ce^{3+}$ in eight and ninefold coordination to oxygen, respectively [20]. The Ce absorption edge for the HIPed zirconolite composition was comprised of an asymmetric doublet, similar in energy position to that of the $CeO_2$ reference compound, inferring that the available Ce inventory remained present as $Ce^{4+}$, analogous to $Pu^{4+}$. A linear combination fit was performed to determine the average oxidation state of Ce, confirming that $93.3 \pm 2\%$ of the Ce remained present as $Ce^{4+}$, inferring an average oxidation state of approximately $Ce^{3.9+}$ (data fit with an R-factor of 0.017). However, powder XRD and SEM data confirmed that considerable unincorporated $CeO_2$ remained present in the microstructure, hence the XANES signal for the HIPed specimen is comprised of contributions from two distinct Ce chemical environments. Nevertheless, as the zirconolite-2M phase accounted for approximately 92 wt% of the overall phase assemblage, it is clear that the dominant oxidation state of Ce in the zirconolite phase is $Ce^{4+}$.

## Conclusions

A sample of zirconolite with nominal composition $Ca_{0.80}Ce_{0.20}ZrTi_{1.60}Cr_{0.40}O_7$ was produced by HIP, with a densification cycle of 1320 °C and 100 MPa maintained for 4 h. The resulting wasteform was characterised by powder XRD, detailing that whilst the target zirconolite-2M phase accounted for $92.3 \pm 0.1$ wt% of the total phase assemblage, a significant fraction of the available Ce inventory, equivalent to approximately 3.9 wt% (acting as a surrogate for Pu) was unincorporated into the zirconolite matrix. SEM–EDS data also revealed the presence of Ce within an accessory perovskite phase, presumably incorporated as $Ce^{3+}$, in line with previous observations. Observations of the interface region between the HIP canister and the bulk ceramic matrix revealed the presence of a Cr-rich oxide layer, with a thickness comparable to those previously detailed for SYNROC that was HIPed in stainless steel canisters. Whilst diffusion of Cr and Fe did not appear to significantly destabilise the phase assemblage at the canister-ceramic interface, Cr was observed to partition within the accessory perovskite phase, potentially providing a charge balancing mechanism permitting greater Ce loading. The formation of a Ce-bearing perovskite expected to be detrimental to the overall wasteform performance. Cr K edge XANES data were consistent with our previous observations, in which $Cr^{3+}$ was largely accommodated in $TiO_6$ octahedra. The Ce $L_3$ XANES spectrum presented features consistent with the $Ce^{4+}$ reference sample, although as a significant portion of the available Ce inventory remained present in the microstructure as $CeO_2$, we do not consider the XANES spectrum obtained to be entirely representative of Ce speciation in the zirconolite phase.

**Acknowledgments** We acknowledge financial support from the Nuclear Decommissioning Authority (NDA) and EPSRC under Grant Numbers EP/S01019X/1, EP/P013600/1 and EP/R511754/1. This research utilised the HADES/MIDAS facility at the University of Sheffield established with financial support from EPSRC and BEIS, under grant EP/T011424/1 [21]. Collection of the Ce $L_3$ and Cr K-edge XAS data was performed under the approval of the Photon Factory Advisory Committee (Proposal No. 2019G586); the support of Yoshihiro Okamoto (Japanese Atomic Energy Agency) and Noriko Usami (The High Energy Accelerator Research Organisation—Kō Enerugī Kasokuki Kenkyū Kikō) during the experiment is gratefully acknowledged.

**Data availability** The data that support these findings cannot be shared at the present time, as they form part of an ongoing study.



## References

1. N.C. Hyatt, Safe management of the UK separated plutonium inventory: a challenge of materials degradation. NPJ Mater. Degrad. (2020). https://doi.org/10.1038/s41529-020-00132-7
2. S.K. Roberts, W.L. Bourcier, H.F. Shaw, Aqueous dissolution kinetics of pyrochlore, zirconolite and brannerite at 25, 50, and 75 °C. Radiochim. Acta **88**(9–11), 539–543 (2000)
3. B.M. Gatehouse, I.E. Grey, R.J. Hill, H.J. Rossell, Zirconolite, $CaZr_xTi_{3-x}O_7$; structure refinements for near-end-member compositions with x = 0.85 and 1.30. Acta Crystallogr. **B37**(1974), 306–312 (1981)
4. L.R. Blackburn et al., Synthesis and characterisation of $Ca_{1-x}Ce_xZrTi_{2-2x}Cr_{2x}O_7$: analogue zirconolite wasteform for the immobilisation of stockpiled UK plutonium. J. Eur. Ceram. Soc. **40**(15), 5909–5919 (2020)
5. G.R. Lumpkin, K.L. Smith, M.G. Blackford, Electron microscope study of Synroc before and after exposure to aqueous solutions. J. Mater. Res. **6**(10), 2218–2233 (1991)
6. S.-K. Sun, M.C. Stennett, C.L. Corkhill, N.C. Hyatt, Reactive spark plasma synthesis of $CaZrTi_2O_7$ zirconolite ceramics for plutonium disposition. J. Nucl. Mater. **500**, 11–14 (2018)
7. L. R. Blackburn et al., Hot isostatically pressed zirconolite wasteforms for actinide immobilization. IOP Conf. Ser. Mater. Sci. Eng. **818**(1), 012010 (2020)
8. S. Thornber, M.C. Stennett, N.C. Hyatt, Investigation of Ce incorporation in zirconolite glass-ceramics for UK plutonium disposition, in 2016 MRS Fall Meeting (2016)

9. S.M. Thornber et al., A preliminary validation study of $PuO_2$ incorporation into zirconolite glass-ceramics. MRS Adv. **1**(4), 1–7 (2018)
10. D.J. Bailey et al., A new approach to the immobilisation of technetium and transuranics: co-disposal in a zirconolite ceramic matrix. J. Nucl. Mater. **528**, 151885 (2019)
11. E. Maddrell, Hot isostatically pressed wasteforms for future nuclear fuel cycles. Chem. Eng. Res. Des. **91**, 735–741 (2013)
12. B.H. Toby, EXPGUI, a graphical user interface for GSAS. J. Appl. Crystallogr. **34**, 210–213 (2001)
13. H. Li, Y. Zhang, P.J. McGlinn, S. Moricca, B.D. Begg, E.R. Vance, Characterisation of stainless steel-synroc interactions under hot isostatic pressing (HIPing) conditions. J. Nucl. Mater. **355**(1–3), 136–141 (2006)
14. Y. Zhang, M.W.A. Stewart, H. Li, M.L. Carter, E.R. Vance, S. Moricca, Zirconolite-rich titanate ceramics for immobilisation of actinides - Waste form/HIP can interactions and chemical durability. J. Nucl. Mater. **395**, 69–74 (2009)
15. Y. Zhang, H. Li, S. Moricca, Pyrochlore-structured titanate ceramics for immobilisation of actinides: Hot isostatic pressing (HIPing) and stainless steel/waste form interactions. J. Nucl. Mater. **377**, 470–475 (2008)
16. L.M. Mottram et al., A feasibility investigation of laboratory based X-ray absorption spectroscopy in support of nuclear waste management. MRS Adv. **XLIII**, 27–35 (2020)
17. S.M. Thornber, L.M. Mottram, A.R. Mason, P. Thompson, C. Stennett, N.C. Hyatt, Solubility, speciation and local environment of chlorine in zirconolite glass–ceramics for the immobilisation of plutonium residues. RSC Adv. **10**, 32497–32510 (2020)
18. D.J. Bailey et al., Ce and U speciation in wasteforms for thermal treatment of plutonium bearing wastes, probed by L3 edge XANES. IOP Conf. Ser. Mater. Sci. Eng. **818**(1), 012019 (2020)
19. M. Tromp, J. Moulin, G. Reid, J. Evans, Cr K-edge XANES spectroscopy: Ligand and oxidation state dependence—what is oxidation state? AIP Conf. Proc. **882**, 699–701 (2007)
20. L.R. Blackburn, S. Sun, L.J. Gardner, E.R. Maddrell, M.C. Stennett, N.C. Hyatt, A systematic investigation of the phase assemblage and microstructure of the zirconolite $CaZr_{1-x}Ce_xTi_2O_7$ system. J. Nucl. Mater. **535**, 152137 (2020)
21. N.C. Hyatt, C.L. Corkhill, M.C. Stennett, R.J. Hand, L.J. Gardner, C.L. Thorpe, The HADES facility for high activity decommissioning engineering & science : part of the UK National Nuclear User Facility. *IOP Conf. Ser. Mater. Sci. Eng.* **818**, 1–8 (2020)